

Demonstration of quadrature interferometric metrology of translation and tilt: QUIMETT

K Nagano ^{1, 2}, K Mori ³, and K Izumi ¹

¹Institute of Space and Astronautical Science, Japan Aerospace Exploration Agency, Sagami-hara, Kanagawa, 252-5210, Japan

²LQUOM, Inc., Yokohama, Kanagawa, 240-8501, Japan

³Hosei University, Koganei, Tokyo, 184-0002, Japan

E-mail: koji.nagano@lquom.com

1 November 2024

Abstract. Future gravitational wave observation in space will demand the improvement on the sensitivity of the local sensor for the drag-free control. This paper presents the proposal, design, and demonstration of a new laser interferometric sensor named Quadrature Interferometric Metrology of Translation and Tilt (QUIMETT) for the drag-free local sensor. QUIMETT enables simultaneous measurements of both translational displacement and tilts of an reflective object with a single interferometer package. QUIMETT offers the characteristic feature where the sensitivity to tilt is independent of the interference condition while maintaining the ability to measure the translational displacement for a range greater than the laser wavelength. The tilt-sensing function has been demonstrated in a prototype experiment. The tilt sensitivity remained unchanged in different interference conditions and stayed at $10 \text{ nrad/Hz}^{1/2}$ at 0.1 Hz.

1. Introduction

Gravitational waves were directly detected for the first time by Advanced Laser Interferometer Gravitational-wave Observatory (LIGO) in 2015 [1, 2]. Currently, the second half of fourth observing run, also known as O4b, by terrestrial gravitational wave antennas including LIGO, Virgo [3] are being performed, and KAGRA [4] will also be taking part in. In the mean time, space gravitational wave antennas including LISA [5], TianQin [6], Taiji [7], and DECIGO [8] have been in development or under consideration. The space gravitational wave antennas will probe gravitational waves oscillating at frequencies lower than a few Hz. Therefore, they are complementary to the terrestrial observatories. The space gravitational wave antennas are anticipated to promote the further research in the field of gravitational wave astronomy and astrophysics.

The space gravitational wave antennas consist of inter-satellite laser interferometers with floating test masses aboard the satellites. The test masses serve as stable references for the gravitational wave observation. To isolate the test masses from noises associated

with the random motion of satellite, the relative distance between the test mass and satellite has to be measured with local sensors and controlled by using the satellite thrusters. This scheme is known as the drag-free control. In the drag-free control, the sensing system often employs the capacitive sensors [9, 10] which offer a wide readout range and a decent displacement sensitivity of typically $\text{nm}/\text{Hz}^{1/2}$ [11] with the hardware in a highly integrated form.

For the space gravitational wave antennas seeking for a higher sensitivity, the improved sensitivity for the local sensors is necessary. For instance, DECIGO requires a displacement sensitivity of $10^{-12} \text{ m}/\text{Hz}^{1/2}$ for the local sensors [12]. A promising sensor concept is the quadrature readout interferometer [13] which provides the displacement measurement of test mass for a range greater than the laser wavelength with a sensitivity better than the capacitive ones. In fact, there have been several research efforts developing the quadrature interferometers for precision measurement applications, such as Homodyne Quadrature Interferometer (HoQI) [14, 15], and modulation-assisted sensors [16, 17, 18, 19]. In addition, various solutions have been proposed to conduct multi-degrees-of-freedom measurement using interferometric sensors for broad applications [20, 21, 22, 23, 24].

Here, we propose a new sensor based on the HoQI scheme, Quadrature Interferometric Metrology of Translation and Tilt (QUIMETT). QUIMETT is a sensor with a simple configuration and no radio-frequency modulation is required, and is intended for use in space due to its resource-saving advantages with multi-degrees-of-freedom measurement in a single unit. QUIMETT adopts the linear combination of two tilt sensor outputs where the interference effect can be compensated to make the tilt sensing independent of the interference condition. This scheme makes QUIMETT capable of measuring the translation and two tilt degrees of freedom simultaneously. We have demonstrated the tilt sensing function and confirmed that the sensitivities do not vary as a function of the interference condition as expected. In this paper, we describe the working principle of the tilt measurement, design of a new optical system dedicated for the demonstration, and experimental verification.

This paper is organized as follows. The principle of operation of the QUIMETT is presented in Section 2. The optical setup of the QUIMETT is given in Section 3. The experimental demonstration of the tilt sensing is presented in Section 4. After discussing the results in Section 5, we conclude this paper in Section 6.

2. Working principles

Figure 1 shows an illustration of conceptual setup for QUIMETT. We begin the analysis by computing the electric fields. Subsequently, the principles of translational displacement and tilt measurements are explained.

element matrices to the input field along the light paths, one can express the electric field vector at PD, \mathbb{E}^{PD} , as

$$\begin{aligned} \mathbb{E}^{\text{PD}} = & \mathbb{B}_h(1) \mathbb{P}(l_2, \eta_2) \mathbb{A}_r \left(\frac{1}{2} \right) \mathbb{P}(l_1, \eta_1) \mathbb{W}^{(2)} \left(-\frac{\pi}{8} \right) \\ & \times \underbrace{\left\{ \mathbb{B}_v(R_{\text{PBS2}}) \mathbb{P}(l_y, \eta_{\text{ITF}}) \mathbb{M}(\Theta_{\text{yaw}}, \Theta_{\text{pitch}}) \mathbb{P}(l_y, \eta_{\text{ITF}_{\text{in}}}) \mathbb{B}_v(R_{\text{PBS2}}) \right\}}_{\text{test mass}} \\ & + \underbrace{\left\{ \mathbb{B}_h(T_{\text{PBS2}}) \mathbb{P}(l_x, \eta_{\text{ITF}}) \mathbb{A}_r(1) \mathbb{P}(l_x, \eta_{\text{ITF}_{\text{in}}}) \mathbb{B}_h(T_{\text{PBS2}}) \right\}}_{\text{reference mirror}} \mathbb{W}^{(2)} \left(\frac{\pi}{8} \right) \mathbb{P}(l_1, \eta_{1_{\text{in}}}) \mathbb{A}_r \left(\frac{1}{2} \right) \mathbb{E}_{\text{in}}, \end{aligned} \quad (2)$$

where \mathbb{A}_r , \mathbb{B}_A , $\mathbb{W}^{(2)}$ and \mathbb{P} are the optical element matrices for non-polarizing reflection, polarizing beamsplitter (PBS), half-wave plate (HWP) and free-space propagation, respectively. The definition of those optical element matrices are given in Appendix A. l and η are the optical path lengths and the Gouy phase shift along optical paths, respectively. The detailed definitions of l and η are shown in Fig. 1 and Tab. 1. Here and hereafter, we assume that l_x and l_y are macroscopically the same and Gouy phase shifts in these path are the same, i.e. $\eta_{x_{\text{in}}} = \eta_{y_{\text{in}}} \equiv \eta_{\text{ITF}_{\text{in}}}$ and $\eta_x = \eta_y \equiv \eta_{\text{ITF}}$. R_{PBS2} and T_{PBS2} are reflectance for vertical polarization and transmittance for horizontal polarization of PBS2, respectively. The matrix \mathbb{M} represents the reflection by the test mass with misalignment in both pitch and yaw directions by the normalized tilts Θ_{yaw} and Θ_{pitch} [25], respectively, as

$$\mathbb{M}(\Theta_{\text{yaw}}, \Theta_{\text{pitch}}) = \mathbb{A}_r(1) + \begin{bmatrix} \hat{M}(\Theta_{\text{yaw}}, \Theta_{\text{pitch}}) & \hat{0} \\ \hat{0} & \hat{M}(\Theta_{\text{yaw}}, \Theta_{\text{pitch}}) \end{bmatrix}, \quad (3)$$

where \hat{A}_r , \hat{M} and $\hat{0}$ are reflection of the mirror, misalignment and zero matrices for each polarization, respectively, the definitions of which are given in Appendix A.

In the same fashion, the electric fields incident upon the two QPDs can be derived as

$$\begin{aligned} \mathbb{E}^{\text{QPD}n} = & \mathbb{F}(n) \mathbb{W}^{(4)} \left(\frac{\pi}{4} \right) \mathbb{P}(l_3, \eta_3) \mathbb{A}_t \left(\frac{1}{2} \right) \mathbb{P}(l_1, \eta_1) \mathbb{W}^{(2)} \left(-\frac{\pi}{8} \right) \\ & \times \underbrace{\left\{ \mathbb{B}_v(R_{\text{PBS2}}) \mathbb{P}(l_y, \eta_{\text{ITF}}) \mathbb{M}(\Theta_{\text{yaw}}, \Theta_{\text{pitch}}) \mathbb{P}(l_y, \eta_{\text{ITF}_{\text{in}}}) \mathbb{B}_v(R_{\text{PBS2}}) \right\}}_{\text{test mass}} \\ & + \underbrace{\left\{ \mathbb{B}_h(T_{\text{PBS2}}) \mathbb{P}(l_x, \eta_{\text{ITF}}) \mathbb{A}_r(1) \mathbb{P}(l_x, \eta_{\text{ITF}_{\text{in}}}) \mathbb{B}_h(T_{\text{PBS2}}) \right\}}_{\text{reference mirror}} \mathbb{W}^{(2)} \left(\frac{\pi}{8} \right) \mathbb{P}(l_1, \eta_{1_{\text{in}}}) \mathbb{A}_r \left(\frac{1}{2} \right) \mathbb{E}_{\text{in}}, \end{aligned} \quad (4)$$

where \mathbb{A}_t is the optical element matrices for non-polarizing transmittance, $\mathbb{W}^{(4)}$ represents a quater-wave plate as defined in Appendix A, and we have introduced \mathbb{F} for selecting the light path between those for QPDs 1 and 2. The definition is given as

$$\mathbb{F}(1) = \mathbb{P}(l_4, \eta_4) \mathbb{B}_h(1), \quad \text{and} \quad \mathbb{F}(2) = \mathbb{P}(l_5, \eta_5) \mathbb{A}_r(1) \mathbb{B}_v(1). \quad (5)$$

Here, we assume that the reflectance and transmittance of PBS3 are unity.

Table 1: Definition of the optical path lengths and the Gouy phase shift along optical paths shown in Fig. 1.

Optical path	Length	Gouy phase shift
NBPS \rightarrow PBS2	l_1	$\eta_{1\text{in}}$
PBS2 \rightarrow Reference mirror	l_x	$\eta_{x\text{in}} (= \eta_{\text{ITF}_{\text{in}}})$
Reference mirror \rightarrow PBS2	l_x	$\eta_x (= \eta_{\text{ITF}})$
PBS2 \rightarrow Floating test mass	l_y	$\eta_{y\text{in}} (= \eta_{\text{ITF}_{\text{in}}})$
Floating test mass \rightarrow PBS2	l_y	$\eta_y (= \eta_{\text{ITF}})$
PBS2 \rightarrow NBPS	l_1	η_1
NPBS \rightarrow PD	l_2	η_2
NPBS \rightarrow PBS3	l_3	η_3
PBS3 \rightarrow QPD1	l_4	η_4
PBS3 \rightarrow QPD2	l_5	η_5

2.2. Translational displacement readout

From Eqs. (2) and (4), the laser intensity of the fundamental Gaussian mode at PD and two QPDs are derived as

$$I_{\text{PD}} = \frac{1 - a \cos 2k(l_x - l_y)}{16} (R_{\text{PBS2}}^2 + T_{\text{PBS2}}^2) P_{\text{in}} + \mathcal{O}(\Theta^2), \quad (6)$$

$$I_{\text{QPD1}} = \frac{1 - a \sin 2k(l_x - l_y)}{16} (R_{\text{PBS2}}^2 + T_{\text{PBS2}}^2) P_{\text{in}} + \mathcal{O}(\Theta^2), \quad (7)$$

$$I_{\text{QPD2}} = \frac{1 + a \sin 2k(l_x - l_y)}{16} (R_{\text{PBS2}}^2 + T_{\text{PBS2}}^2) P_{\text{in}} + \mathcal{O}(\Theta^2), \quad (8)$$

where $\mathcal{O}(\cdot)$ is the Landau symbol, k is the wave number, and a denotes the visibility, defined by $a = 2R_{\text{PBS2}}T_{\text{PBS2}}/(R_{\text{PBS2}}^2 + T_{\text{PBS2}}^2)$. Here, we only consider the visibility degradation caused by imbalance in PBS2 while other factors are ignored, such as misalignment in HWP, spatial mode mismatching, losses in the Michelson part.

Combining these three signals, one can readout the translational displacement for an extended range. For example, one can plug the measurement values into the function [14],

$$\frac{I_{\text{PD}} - I_{\text{QPD2}}}{I_{\text{PD}} - I_{\text{QPD1}}} = \tan \left(2k(l_x - l_y) + \frac{\pi}{4} \right), \quad (9)$$

and retrieve the displacement by applying the arc-tangent operation. This highlights the advantage of quadrature readout interferometer where the range of translational displacement can be expanded to a range greater than the wavelength via an additional signal processing. QUIMETT maintains this ability since I_{QPD1} (I_{QPD2}) can be measured with the sum signal of all segments in QPD1 (QPD2).

2.3. Tilt readout

The QPDs play a crucial role in deriving the information associated with the tilts. The tilt information for the yaw (pitch) direction can be readily obtained by taking the difference in light intensities between the left and right (upper and lower) segments. This results in tilt signal in the form of

$$I_{\text{QPD1}}^{\text{tilt}} = \frac{\Theta_B R_{\text{PBS2}}}{2\sqrt{2\pi}} [-T_{\text{PBS2}} \cos \{2k(l_x - l_y) - \eta_{\text{ITF}} - \eta_{\text{QPD1}}\} + R_{\text{PBS2}} \sin(\eta_{\text{ITF}} + \eta_{\text{QPD1}})] P_{\text{in}}, \quad (10)$$

$$I_{\text{QPD2}}^{\text{tilt}} = \frac{\Theta_B R_{\text{PBS2}}}{2\sqrt{2\pi}} [T_{\text{PBS2}} \cos \{2k(l_x - l_y) - \eta_{\text{ITF}} - \eta_{\text{QPD2}}\} + R_{\text{PBS2}} \sin(\eta_{\text{ITF}} + \eta_{\text{QPD2}})] P_{\text{in}}, \quad (11)$$

$$\eta_{\text{QPD1}} \equiv \eta_1 + \eta_3 + \eta_4, \quad \eta_{\text{QPD2}} \equiv \eta_1 + \eta_3 + \eta_5, \quad (12)$$

where B is any tilt in pitch or yaw, and Eqs. (10) and (11) give the response to the tilt in the direction selected at B .

It is now evident with Eqs. (10) and (11) that the ordinary signal extraction with QPD is strongly influenced by the interference condition or more specifically the length difference $l_x - l_y$. Therefore, these signals do not directly appear to be suitable for precise tilt measurements.

We propose introducing the sum of two tilt signals, Eqs. (10) and (11),

$$I_{\text{QPD1}}^{\text{tilt}} + I_{\text{QPD2}}^{\text{tilt}} = \frac{\Theta_B R_{\text{PBS2}}^2}{2\sqrt{2\pi}} [\sin(\eta_{\text{ITF}} + \eta_{\text{QPD1}}) + \sin(\eta_{\text{ITF}} + \eta_{\text{QPD2}})] P_{\text{in}} \quad (13)$$

$$= \frac{\Theta_B R_{\text{PBS2}}^2 \sin(\eta_{\text{ITF}} + \eta_{\text{QPD}})}{\sqrt{2\pi}} P_{\text{in}}. \quad (14)$$

Here and hereafter, we assume that l_4 and l_5 are the same and, consequently, $\eta_4 = \eta_5$ and $\eta_{\text{QPD1}} = \eta_{\text{QPD2}} \equiv \eta_{\text{QPD}}$. The tilts along both measurement axes of the target can be directly determined, independent of interference effect $l_x - l_y$. Note that the effect of the reference mirror tilt is discussed in Appendix B.

3. Experimental setup

The experimental setup for demonstration of tilt measurement with QUIMETT is illustrated in Fig. 2. In this experiment, a laser source, Mephisto S200 of Coherent Inc., was employed with the wavelength of 1064 nm. The free space output from the laser source is coupled to a single-mode optical fiber and introduced to the fiber collimator on the optical bench. The input power at NPBS is adjusted to be 1.6 mW. The QPDs are G6849 from Hamamatsu Photonics. All the optical components except for two end mirrors are mounted on an aluminum plate. The mirror simulating the test mass is a broadband dielectric mirror with a diameter of 19 mm from Thorlabs, and the other optical elements are designed to have 1/2 inch in diameter.

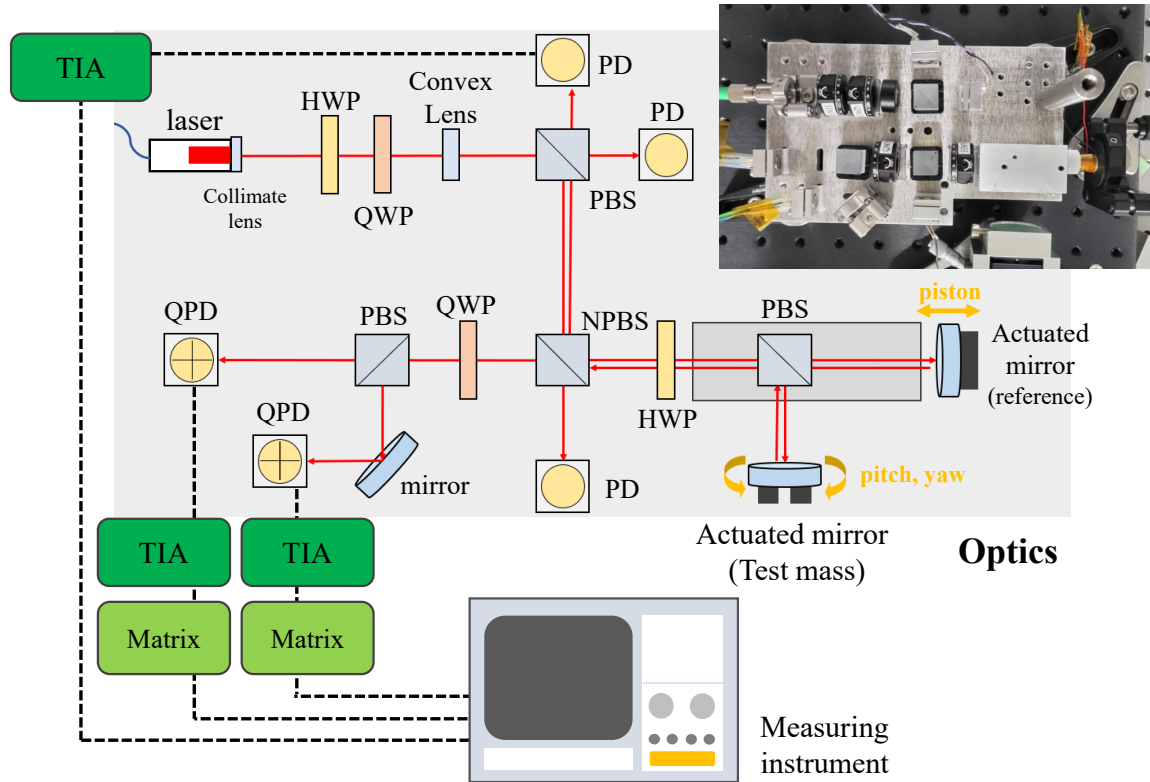


Figure 2: Optical layout used in the experiment. A photograph in the upper right corner shows the actual setup. The actuated mirror at the bottom simulates the tilt of test mass while the one on the right of PBS adjusts the interference condition. The yellow texts and accompanying arrows illustrate the direction of motion for the actuator coupled to the mirrors.

A convex lens is inserted in the optical system for two reasons. First, the lens keeps the beam size small enough throughout the system so that it does not require an additional train of lenses. The other reason is that it adjusts the Gouy phase evolution. As discussed in Sec. 2, the response to tilt deviations depends on the Gouy phase accumulated from the test mass to the locations of QPDs. If not carefully designed, the tilt signal would vanish in the worst case. We avoid such a situation by designing the beam waist locating in the vicinity of the test mass. In our experiment, the beam waist is measured to be 15 mm behind the test mass. The Gouy phase from the test mass to the QPDs is measured to be 106 deg.

All the QPDs and PDs are connected to the transimpedance amplifiers (TIAs) via lead wires. The TIAs are mounted on a separate location. The voltage signals coming out of the TIAs are continuously recorded in time series. The measurement instrument is YOKOGAWA DL850E with 16bit modules.

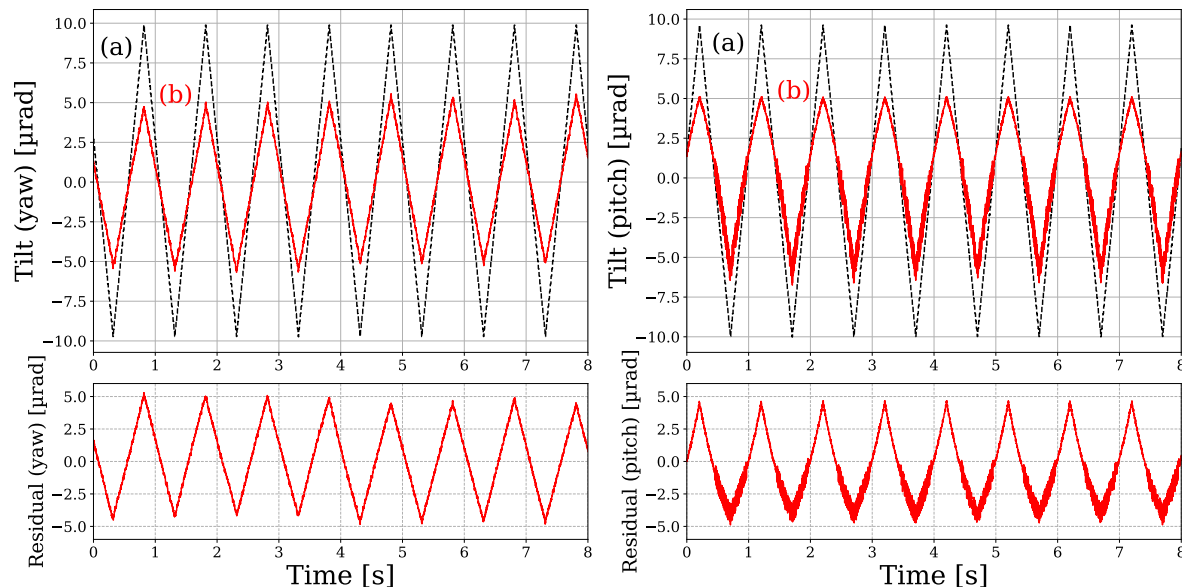


Figure 3: Comparison of theoretical (a) and actual (b) tilt measurement results for yaw and pitch directions in bright fringe. The theoretical traces are based on Eq. (14), described in Sec. 2. The left figure shows the yaw measurements, and the right figure shows the pitch measurements.

4. Experimental Demonstrations

4.1. Tilt Measurement

As discussed in Sec. 2, the critical function in QUIMETT is the tilt sensing which is designed to be independent of the interference condition. To experimentally demonstrate this function, the tilt measurements were repeated over four different interference conditions in QPD1 as follows.

$$2k(l_x - l_y) = \begin{cases} \pi N & (\text{mid}(-)) \\ \pi N + \pi/4 & (\text{dark}) \\ \pi N + \pi/2 & (\text{mid}(+)) \\ \pi N + 3\pi/4 & (\text{bright}) \end{cases} \quad (15)$$

We hereafter call those interference conditions, $\text{mid}(-)$, dark, $\text{mid}(+)$, and bright. The interference condition was adjusted by the piezo actuator on the reference mirror.

During the measurements, the tilt of the test mass simulator was excited by triangular waves at 1 Hz with an amplitude of $10 \mu\text{rad}$. The triangular waves were generated by a function generator and sent to the set of piezo actuators driving the test mass simulator as shown in Fig. 2. The pitch and yaw excitations are applied one at a time.

The results of tilt measurements for yaw and pitch directions in the bright fringe are shown in Fig. 3 together with the theoretical values for comparison. The measured

voltage data are calibrated to the tilt data using Eq. (14). In this calculation, we assume $R_{\text{PBS2}} = 1$ and $T_{\text{PBS2}} = 1$ and we use the parameters shown in Tab. 2. In both yaw and pitch directions, the measured values are found to be almost half of the theoretical expectation values. However, the tilt motions are measured consistently during the measurement time. Some discrepancy could be due to the uncharacterized optical losses in the optics in the actual setup. The tilt measurement and residual show the same waveform, indicating that there is not large distortion in the measurement but a difference in scaling factor.

Table 2: Parameters used to calculate the theoretical output of the pitch and yaw signals shown in Figs. 3 and 4.

Parameters	Values
Input power (P_{in})	1.6 mW
Gouy phase ($\eta_{\text{TF}} + \eta_{\text{QPD}}$)	106 deg
Response of QPDs	0.68 A/W
Trans-impedance gain of QPDs	4700 V/A
Beam size on the actuated mirror	116 μm

Similarly, the results of the tilt measurements for the other three interference conditions are shown in Fig. 4. It is clear that the tilt motion can be measured in three fringe conditions in addition to the mid(-). Therefore, QUIMETT can read out the tilts without an influence from the interference condition as expected.

4.2. Tilt measurement noise

The noise measurement was performed to assess the practical sensitivity with QUIMETT under the four interference conditions (15). The recorded time series were converted into the amplitude spectral density via the Welch’s estimation technique with the hann window applied. The frequency band was set to 0.01-100 Hz, which is relevant to the space gravitational wave antennas. The amplitude spectral densities of noise in four different interference conditions are shown in Fig. 5.

In addition, an extra measurement was performed with the mirror in the optical system replaced with a mirror mounted on a standard mount to see the influence from the piezo-actuated mirror. The data is shown with label (a) in Fig. 5.

In any interference conditions, sharp features are seen at frequencies above 10 Hz. These noise features increases in the mid fringes. On the other hand, we find the noise levels to be almost identical between the different interference conditions at frequencies below 10 Hz. We determined this noise to be the digitization noise from the data recorder as shown in Fig. 6. In fact, the tilt sensing noise above 10 Hz is almost entirely dominated by the digitization noise.

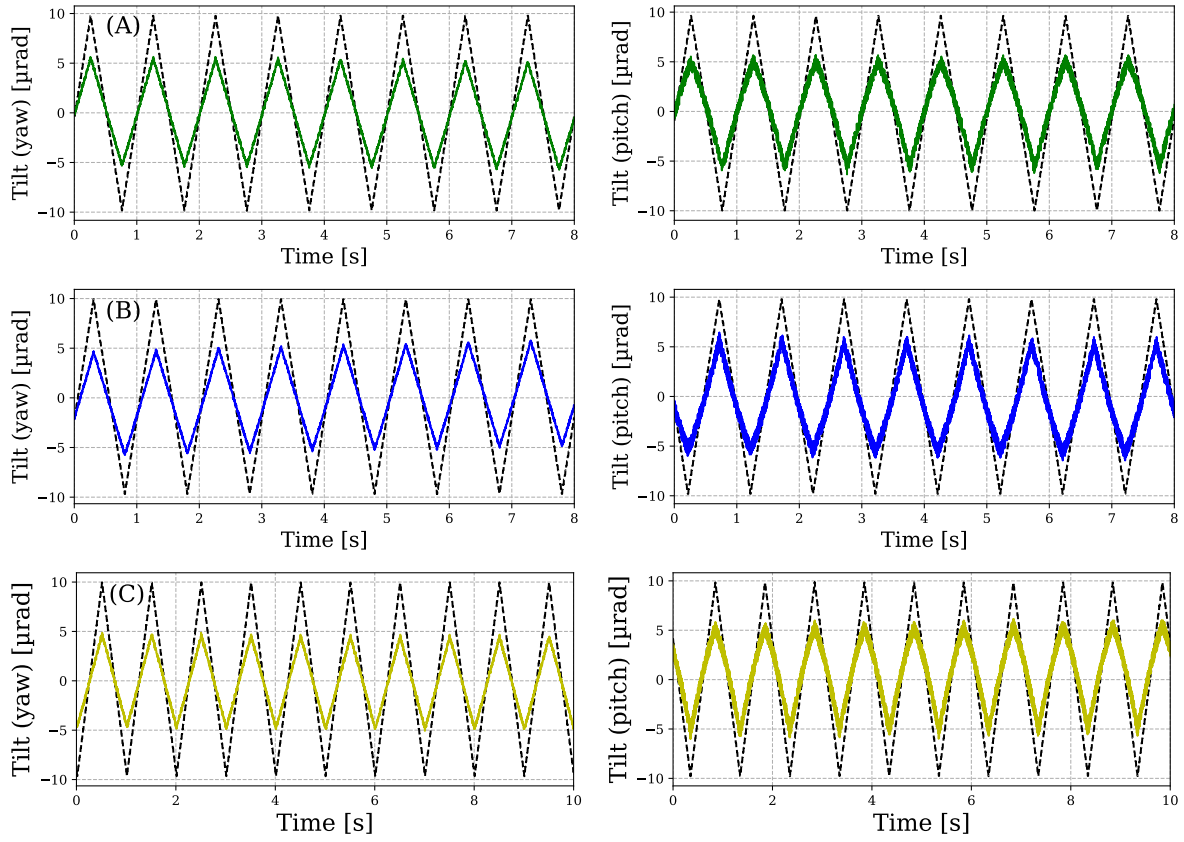


Figure 4: Tilt measurements at different interference conditions. (A) shows mid(+) fringe, (B) shows dark fringe, and (C) shows mid(-) fringe.

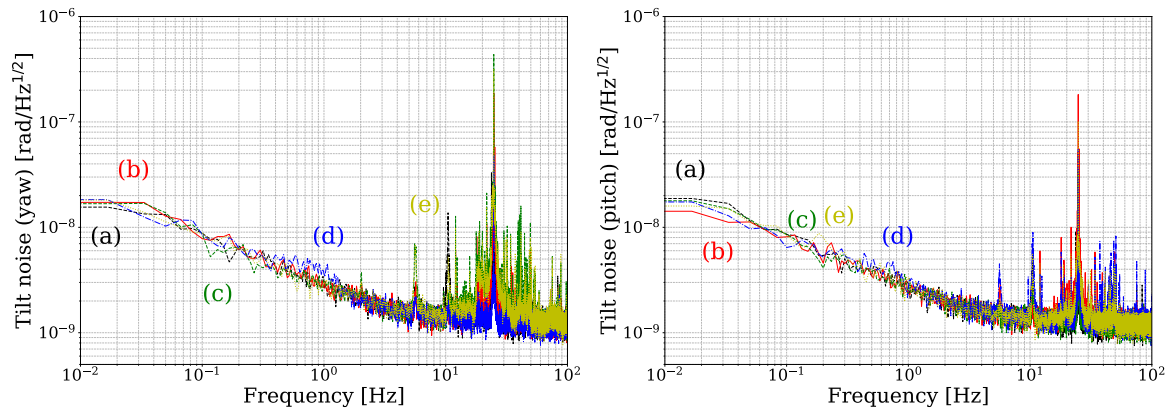


Figure 5: Tilt noises in amplitude spectral densities. Measurements are performed at four interference conditions. (b) shows bright fringe, (c) shows mid(+), (d) shows dark fringe, and (e) shows mid(-). The measurement results without the piezoelectric element (a) are also shown to evaluate the effect of the piezoelectric element.

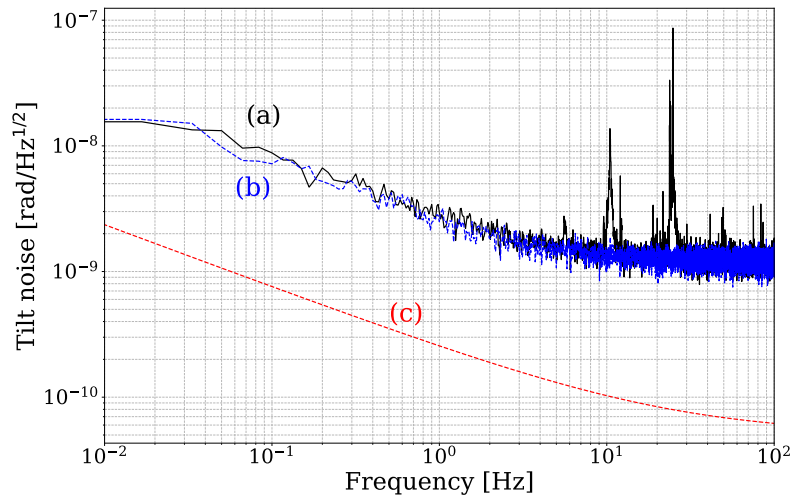


Figure 6: Noise budget for tilt noises. (a) shows the tilt sensing noise obtained with a fixed mirror, (b) shows the ADC noise associated with the measurement instrument and (c) shows electronic noise by the TIA and matrix electronics.

5. Discussions

Besides the demonstration of the tilt measurement, there are several critical considerations which have to be addressed before adopting QUIMETT as the local sensor for the drag-free control. First, a further look into the length-to-tilt coupling is necessary. As described in Sec. 4, the response to tilts did not change as the function of the interference condition. However, there could be unexpected cross-coupling where the dynamical motion in the length degree of freedom leak into the tilt signals. We were not able to quantify such couplings in this setup because the piezo-actuated mirror showed an inherent cross-coupling between the tilts and length presumably due to the mechanical imbalance.

Similarly, the tilt-to-length coupling must be studied. As shown in Eq. (9), the length signal is immune to the variation in the light intensity. This holds true as long as the responsibilities of the PD and QPDs do not vary. However, the total amount of light detected by the QPDs could easily be a function of the beam spot displacement caused by the test mass tilts because the QPDs are inherently more sensitive to this coupling due to the fact that there are gaps between the segments where the light is not converted into the photocurrent. Such a tilt-to-length coupling can also occur in the single-element PD due to the inhomogeneous responsibility across the PD surface area, but it is typically smaller than that of the QPDs.

Furthermore, comparing against the single-element PDs, the use of QPDs tends to reduce the signal-to-noise ratio for length sensing due to the presence of the gap between the segments. This could lead to a situation where the level of noise floor in the length measurement varies depending on the spot position on QPDs. This may impact on the background noise estimation in gravitational wave data analysis where the stationary

noise over a long time scale is often preferable.

As shown in Eqs. (10) and (11), each QPD signal contains not only the tilt component but also the one associated with the length difference or $l_x - l_y$. Consequently the electronics and measurement instrument have to deal with a wide range of signals. In the current setup, the tilt signals of each QPD were recorded by the measurement instrument and subsequently the sum of the two QPD signals was computed in the post process. This made the contribution of ADC noise particularly large due to the relatively narrow dynamic range in the ADC. Therefore, we can improve the noise floor by introducing analog electronics such that the summing process is completed before the ADC where the ADC range can be adjusted to be a smaller value.

Finally, refinement of the optical design to reduce the volume and weight for the space application is necessary. Equation (14) reveals that optical path length does not influence the tilt sensitivity. This means the reduction of the optical path lengths enables a design with smaller volume without compromising the sensitivity. In particular, shortening the distance between PBS1 and NPBS in the Fig. 1 is considered to be effective for achieving a compact design.

6. Conclusion

This paper proposes a new local sensor concept for the drag-free control in space. The sensor is based on the quadrature interferometer and named QUIMETT. QUIMETT enables the simultaneous readout of both translation and tilt degrees of freedom using a single interferometer module. This paper presented for the first time the working principle of the tilt measurements and its demonstration by building the dedicated optical system. In the experimental verification, the main focus was put on the demonstration of the tilt readout which were designed to be independent of the interference condition. The experimental demonstration successfully confirmed this function. The tilt sensitivity currently marks $10 \text{ nrad/Hz}^{1/2}$ at 0.1 Hz and did not change in four different interference conditions as expected. We discussed the studies which have to be further looked in before considering this scheme as a viable solution for the drag-free control.

Acknowledgment

We thank Advanced Machining Technology Group and K. Komori for technical support, thank C. M. Mow-Lowry and S. Sato for useful discussions. This project was supported by JSPS KAKENHI Grant Number JP20J01928 and JP22K14067. K.N. is an employee of LQUOM, Inc.

Author contributions

K.N. and K.M. carried out the experiment. K.N. conceived the original idea. K.M. and K.I. developed the theoretical formalism, and performed the analytic calculations. K.I. supervised the project. All authors discussed the results and contributed to the final manuscript. K.N. and K.M. contribute equally the presented work.

Appendix A. Mathematical foundation

Here, we show the mathematical background of the optical analysis in this paper. Upon transmission and reflection, the electric field in a polarization acquire sets of coefficients given matrix form as,

$$\hat{t}(T) = \sqrt{T} \text{diag}(1, 1, 1) \quad \text{and} \quad \hat{r}(R) = \sqrt{R} \text{diag}(1, -1, 1), \quad (\text{A.1})$$

where diag represents the diagonal matrix, T and R are the transmittance and reflectance of the optic, respectively. Using these matrices, one can express the polarizing beam splitter (PBS) in the 6×6 format as

$$\mathbb{B}_h(T) = \begin{bmatrix} \hat{t}(T) & \hat{0} \\ \hat{0} & \hat{0} \end{bmatrix} \quad \text{and} \quad \mathbb{B}_v(R) = \begin{bmatrix} \hat{0} & \hat{0} \\ \hat{0} & \hat{r}(R) \end{bmatrix}. \quad (\text{A.2})$$

\mathbb{B}_t is transmission of PBS, and \mathbb{B}_v is reflection of PBS. Similarly, reflection and transmission of optical elements are expressed as

$$\mathbb{A}_t(T) = \begin{bmatrix} \hat{t}(T) & \hat{0} \\ \hat{0} & \hat{t}(T) \end{bmatrix} \quad \text{and} \quad \mathbb{A}_r(R) = \begin{bmatrix} -\hat{r}(R) & \hat{0} \\ \hat{0} & \hat{r}(R) \end{bmatrix}. \quad (\text{A.3})$$

We deal with misalignment of optical element [25] as an additive matrix as

$$\hat{M}(\Theta_{\text{yaw}}, \Theta_{\text{pitch}}) = \begin{bmatrix} 0 & -2i\Theta_{\text{yaw}} & -2i\Theta_{\text{pitch}} \\ -2i\Theta_{\text{yaw}} & 0 & 0 \\ -2i\Theta_{\text{pitch}} & 0 & 0 \end{bmatrix}, \quad (\text{A.4})$$

where Θ_A represents the normalized tilt defined by $\Theta_A = (\theta_A \pi \omega(z)) / \lambda$ with θ_A a rotation in the optic, λ the wavelength and $w(z)$ the beam radius at the propagation point z . Eq. (A.4) is only valid when Θ_A is sufficiently small. The propagation for by optical path transmission is represented as

$$\mathbb{P}(l, \eta) = e^{-ikl} \mathbb{R}(\eta), \quad (\text{A.5})$$

where l is the distance from one location to another, η is the Gouy phase shift in the optical path, and k is the wave number. The Gouy phase shift matrix $\mathbb{R}(\eta)$ is expressed as

$$\mathbb{R}(\eta) = \begin{bmatrix} \hat{R}(\eta) & \hat{0} \\ \hat{0} & \hat{R}(\eta) \end{bmatrix} \quad \text{where} \quad \hat{R}(\eta) = \text{diag}(1, e^{-i\eta}, e^{-i\eta}). \quad (\text{A.6})$$

The half wave plate can be expressed as [26]

$$\mathbb{W}^{(2)}(\phi) = \begin{bmatrix} \hat{H}(\phi) & \hat{H}(\frac{\pi}{4} - \phi) \\ \hat{H}(\frac{\pi}{4} - \phi) & -\hat{H}(\phi) \end{bmatrix}, \quad \text{where} \quad \hat{H}(\phi) = \cos 2\phi \hat{I}, \quad (\text{A.7})$$

with ϕ the angle between the fast axis to half wave plate. Jones matrix of quarter wave plate is:

$$\mathbb{W}^{(4)}(\psi) = \begin{bmatrix} \frac{1+i}{2} \hat{I} + \hat{Q}(\frac{\pi}{4} - \psi) & \hat{Q}(\psi) \\ \hat{Q}(\psi) & \frac{1+i}{2} \hat{I} - \hat{Q}(\frac{\pi}{4} - \psi) \end{bmatrix}, \quad \text{where} \quad \hat{Q}(\psi) = \frac{1-i}{2} \sin 2\psi \hat{I}, \quad (\text{A.8})$$

where ψ is angular of quarter wave plate to fast axis.

The total intensity of laser falling onto a PD or QPDs can be calculated as

$$I^{\text{sum}} = \sum_{A=h,v} \left(\vec{E}^A \right)^\dagger \vec{E}^A. \quad (\text{A.9})$$

For tilt sensing by the QPDs, using the laser intensity in the hemisphere of the QPD. For detect tilt in the yaw direction, the laser intensity in the left and right half is discussed here. We hereafter consider one polarization mode since, in the setup of QUIMETT, the QPDs detect one polarized light due to the PBS in front of the QPDs. Laser intensity of the right half of the QPD is denoted as

$$S^{(\text{r.h.})} = \int_0^\infty |\vec{E}|^2 dx = \int_0^\infty |E_{00}U_{00} + E_{10}U_{10} + E_{01}U_{01}|^2 dx \quad (\text{A.10})$$

$$= \frac{1}{2} |E_{00}|^2 + \left[E_{00}E_{10}^* \int_0^\infty U_{00}U_{10}^* dx + (\text{c.c.}) \right] + (\text{vertical mode term}), \quad (\text{A.11})$$

where x represents horizontal position on the QPD, and U_{00} and U_{10} (U_{01}) represent the fundamental and first-order Hermite polynomial denoting the horizontally (vertically) spatial mode of the Gaussian-Hermite beam, respectively. Here, we assume that $|E_{00}| \gg |E_{10/01}|$ and the size of the QPD is much larger than the beam size on the QPD. U_{00} and U_{10} are defined as

$$U_{00} = \left(\frac{2}{\pi} \right)^{\frac{1}{4}} \frac{1}{\sqrt{\omega}} \exp \left[-x^2 \left(\frac{1}{\omega^2} + i \frac{k}{2R} \right) \right] \quad \text{and} \quad U_{10} = \frac{2x}{\omega} U_{00}, \quad (\text{A.12})$$

where ω and R are beam size and curvature of the electric field on the QPD, respectively. From this definition, we can obtain the following equation,

$$\begin{aligned} \int_0^\infty U_{00}U_{10}^* dx &= \left(\frac{2}{\pi} \right)^{\frac{1}{2}} \frac{2}{\omega^2} \int_0^\infty x \exp \left(-\frac{2x^2}{\omega^2} \right) dx \\ &= \frac{1}{\sqrt{2\pi}}. \end{aligned} \quad (\text{A.13})$$

Also this is true for the complex conjugated one, so that

$$\int_0^\infty U_{00}U_{10}^*dx = \int_0^\infty U_{00}^*U_{10}dx = \frac{1}{\sqrt{2\pi}}. \quad (\text{A.14})$$

As a result, Eq. (A.11) is denoted as

$$S^{(\text{r.h.})} = \frac{1}{2}|E_{00}|^2 + \sqrt{\frac{2}{\pi}}\Re[E_{00}E_{10}^*] + (\text{vertical mode term}). \quad (\text{A.15})$$

Similarly, the left half is:

$$S^{(\text{l.h.})} = \frac{1}{2}|E_{00}|^2 - \sqrt{\frac{2}{\pi}}\Re[E_{00}E_{10}^*] + (\text{vertical mode term}). \quad (\text{A.16})$$

Tilt sensing by QPD is provided by subtraction of one hemisphere from the other,

$$S^{\text{yaw}} = S^{(\text{r.h.})} - S^{(\text{l.h.})} = \sqrt{\frac{8}{\pi}}\Re[E_{00}E_{10}^*]. \quad (\text{A.17})$$

Substituting E_{01}^* (vertical mode) for E_{10}^* (horizontal mode) in Eq. (A.17) allows us to derive the pitch tilt detection value.

Appendix B. Effect of reference mass

Here, we study the case of tilting $\Theta_{\text{yaw}2}$, and $\Theta_{\text{pitch}2}$ of the reference mirror. Under this condition, the electric field incident upon the two QPDs can be derived as

$$\begin{aligned} \mathbb{E}^{\text{QPD}n} = & \mathbb{F}(n)\mathbb{W}^{(4)}\left(\frac{\pi}{4}\right)\mathbb{P}(l_3, \eta_3)\mathbb{A}_t\left(\frac{1}{2}\right)\mathbb{P}(l_1, \eta_1)\mathbb{W}^{(2)}\left(-\frac{\pi}{8}\right) \\ & \times \{\mathbb{B}_v(R_{\text{PBS}2})\mathbb{P}(l_y, \eta_{\text{ITF}})\mathbb{M}(\Theta_{\text{yaw}}, \Theta_{\text{pitch}})\mathbb{P}(l_y, \eta_{\text{ITF}_{\text{in}}})\mathbb{B}_v(R_{\text{PBS}2}) \\ & + \mathbb{B}_h(T_{\text{PBS}2})\mathbb{P}(l_x, \eta_{\text{ITF}})\mathbb{M}(\Theta_{\text{yaw}2}, \Theta_{\text{pitch}2})\mathbb{P}(l_x, \eta_{\text{ITF}_{\text{in}}})\mathbb{B}_h(T_{\text{PBS}2})\} \\ & \times \mathbb{W}^{(2)}\left(\frac{\pi}{8}\right)\mathbb{P}(l_1, \eta_{1_{\text{in}}})\mathbb{A}_r\left(\frac{1}{2}\right)\mathbb{E}_{\text{in}}. \end{aligned} \quad (\text{B.1})$$

The tilt signal of QUIMETT is

$$I_{\text{QPD}1}^{\text{tilt}} + I_{\text{QPD}2}^{\text{tilt}} = \frac{(\Theta_{B2}T_{\text{PBS}2}^2 + \Theta_B R_{\text{PBS}2}^2)\sin(\eta_{\text{ITF}} + \eta_{\text{QPD}})}{\sqrt{2\pi}}P_{\text{in}}. \quad (\text{B.2})$$

Equation (B.2) shows the tilts of the two mirrors are inseparable. Therefore, it is important to mount the reference mirror securely for precise tilt measurement.

References

- [1] Junaid Aasi, BP Abbott, Richard Abbott, Thomas Abbott, MR Abernathy, Kendall Ackley, Carl Adams, Thomas Adams, Paolo Addresso, RX Adhikari, et al. Advanced ligo. *Class. Quantum Grav.*, 32(7):074001, 2015.

- [2] Benjamin P Abbott, Richard Abbott, TDe Abbott, MR Abernathy, Fausto Acernese, Kendall Ackley, Carl Adams, Thomas Adams, Paolo Addesso, Rana X Adhikari, et al. Observation of gravitational waves from a binary black hole merger. *Physical review letters*, 116(6):061102, 2016.
- [3] Fet al Acernese, M Agathos, K Agatsuma, Damiano Aisa, N Allemandou, Aea Allocca, J Amarni, Pia Astone, G Balestri, G Ballardini, et al. Advanced virgo: a second-generation interferometric gravitational wave detector. *Classical and Quantum Gravity*, 32(2):024001, 2014.
- [4] Kentaro Somiya and KAGRA Collaboration. Detector configuration of kagra—the japanese cryogenic gravitational-wave detector. *Classical and Quantum Gravity*, 29(12):124007, 2012.
- [5] Pau Amaro-Seoane, Heather Audley, Stanislav Babak, John Baker, Enrico Barausse, Peter Bender, Emanuele Berti, Pierre Binetruy, Michael Born, Daniele Bortoluzzi, et al. Laser interferometer space antenna. *arXiv preprint arXiv:1702.00786*, 2017.
- [6] Jun Luo, Li-Sheng Chen, Hui-Zong Duan, Yun-Gui Gong, Shoucun Hu, Jianghui Ji, Qi Liu, Jianwei Mei, Vadim Milyukov, Mikhail Sazhin, et al. Tianqin: a space-borne gravitational wave detector. *Classical and Quantum Gravity*, 33(3):035010, 2016.
- [7] Wen-Hong Ruan, Zong-Kuan Guo, Rong-Gen Cai, and Yuan-Zhong Zhang. Taiji program: Gravitational-wave sources. *International Journal of Modern Physics A*, 35(17):2050075, 2020.
- [8] Seiji Kawamura, Masaki Ando, Naoki Seto, Shuichi Sato, Takashi Nakamura, Kimio Tsubono, Nobuyuki Kanda, Takahiro Tanaka, Jun'ichi Yokoyama, Ikkoh Funaki, et al. The japanese space gravitational wave antenna: Decigo. *Classical and Quantum Gravity*, 28(9):094011, 2011.
- [9] M Armano, H Audley, G Auger, J Baird, P Binetruy, M Born, Daniele Bortoluzzi, N Brandt, A Bursi, M Caleno, et al. The lisa pathfinder mission. In *Journal of Physics: Conference Series*, volume 610, page 012005. IOP Publishing, 2015.
- [10] V Josselin, P Touboul, and R Kielbasa. Capacitive detection scheme for space accelerometers applications. *Sensors and Actuators A: Physical*, 78(2-3):92–98, 1999.
- [11] M Armano, H Audley, G Auger, J Baird, M Bassan, P Binetruy, M Born, D Bortoluzzi, N Brandt, M Caleno, et al. Capacitive sensing of test mass motion with nanometer precision over millimeter-wide sensing gaps for space-borne gravitational reference sensors. *Physical review D*, 96(6):062004, 2017.
- [12] Koji Nagano. *Control scheme for a Fabry–Pérot type interferometric space gravitational wave antenna*. PhD thesis, Ph. D. Thesis, 2020.
- [13] GMB Bouricius and SF Clifford. An optical interferometer using polarization coding to obtain quadrature phase components. *Review of Scientific Instruments*, 41(12):1800–1803, 1970.
- [14] Sam J Cooper, Chris J Collins, Anna C Green, David Hoyland, CC Speake, Andreas Freise, and CM Mow-Lowry. A compact, large-range interferometer for precision measurement and inertial sensing. *Classical and Quantum Gravity*, 35(9):095007, 2018.
- [15] SJ Cooper, CJ Collins, L Prokhorov, J Warner, D Hoyland, and CM Mow-Lowry. Interferometric sensing of a commercial geophone. *Classical and Quantum Gravity*, 39(7):075023, 2022.
- [16] Gerhard Heinzl, Felipe Guzmán Cervantes, Antonio F García Marín, Joachim Kullmann, Wang Feng, and Karsten Danzmann. Deep phase modulation interferometry. *Optics express*, 18(18):19076–19086, 2010.
- [17] Oliver Gerberding. Deep frequency modulation interferometry. *Optics express*, 23(11):14753–14762, 2015.
- [18] Daniel A Shaddock. Digitally enhanced heterodyne interferometry. *Optics letters*, 32(22):3355–3357, 2007.
- [19] Andrew J Sutton, Oliver Gerberding, Gerhard Heinzl, and Daniel A Shaddock. Digitally enhanced homodyne interferometry. *Optics express*, 20(20):22195–22207, 2012.
- [20] Hung-Lin Hsieh and Ssu-Wen Pan. Development of a grating-based interferometer for six-degree-of-freedom displacement and angle measurements. *Optics express*, 23(3):2451–2465, 2015.
- [21] Hao Yan, Hsien-Chi Yeh, and Qiuli Mao. High precision six-degree-of-freedom interferometer for test mass readout. *Classical and Quantum Gravity*, 39(7):075024, 2022.

- [22] Yichao Yang, Kohei Yamamoto, Victor Huarcaya, Christoph Vorndamme, Daniel Penkert, Germán Fernández Barranco, Thomas S Schwarze, Moritz Mehmet, Juan Jose Esteban Delgado, Jianjun Jia, et al. Single-element dual-interferometer for precision inertial sensing. *Sensors*, 20(17):4986, 2020.
- [23] Neda Meshksar, Moritz Mehmet, Katharina-Sophie Isleif, and Gerhard Heinzl. Applying differential wave-front sensing and differential power sensing for simultaneous precise and wide-range test-mass rotation measurements. *Sensors*, 21(1):164, 2020.
- [24] Xin Xu, Jinsong Liu, Henglin Mu, Yan Li, and Yidong Tan. Six-degrees-of-freedom test mass readout via optical phase-locking heterodyne interferometry. *IEEE Transactions on Instrumentation and Measurement*, 73:1–7, 2024.
- [25] Yaron Hefetz, Nergis Mavalvala, and Daniel Sigg. Principles of calculating alignment signals in complex resonant optical interferometers. *JOSA B*, 14(7):1597–1606, 1997.
- [26] R Clark Jones. A new calculus for the treatment of optical systems i. description and discussion of the calculus. *Josa*, 31(7):488–493, 1941.